Developing meshing workflows in GMSH v4.11 for Geologic Uncertainty Assessment of the High-Temperature Aquifer Thermal Energy Storage

Ali Dashti[1], Jens C. Grimmer[1], Christophe Geuzaine[2], Florian Bauer[3], Thomas Kohl[1]

[1]Institute of Applied Geosciences, Karlsruhe Institute of Technology (KIT), Karlsruhe, Germany
[2]Université de Liège, Institut Montefiore B28, 4000 Liège, Belgium
[3]Institute for Nuclear Waste Disposal, Karlsruhe Institute of Technology (KIT), Hermann-von-Helmholtz-Platz 1, 76344 Eggenstein-Leopoldshafen, Germany

Correspondence to: Ali Dashti (Ali.dashti@kit.edu)

Abstract. Evaluating uncertainties of geological features on temperature and pressure changes in the reservoir's fluids plays a crucial role~~are crucial~~ for a safe and sustainable operation of the High-Temperature Aquifer Thermal Energy Storage (HT-ATES). This study uses a new automated surface fitting function in the Python API of GMSH (v. 4.11) to model the impact of arbitrary structural barriers and variations of roof and floor geometries on temperature and pressure in heat storage applications. A Python workflow is developed ~~in Python~~ to implement an automated mesh generation routine for varying geological scenarios ~~that cannot be predicted by surface-based exploration methods~~. This way, the geological models and their ~~underlying~~ inherent uncertainties are transferred into reservoir simulations. We applied our ~~modelling~~ modelling approaches on two case studies: 1) Greater Geneva Basin with the Upper Jurassic ("Malm") limestone reservoir of 100 m thickness and 2) the DeepStor project in the Upper Rhine Graben with an Oligocene sandstone reservoir of 10 m thickness. In the Greater Geneva Basin showcase, the ~~upper~~ top and ~~lower~~ bottom surfaces of the reservoir are shifted ± ~~8~~ 10 and ± ~~10~~ 15 m, respectively to ~~perturb~~ vary ~~topology~~ the geometry of the thick reservoir. ~~Independence~~ The heat plume is independent of the reservoir geometry, indicating~~of the heat plume from reservoir´s topology indicates~~ the limited propagation of the induced thermal regime in thick reservoirs and redundancy of the advanced exploration campaigns like 3D seismic. In DeepStor, an arbitrary sub-seismic fault juxtaposing the permeable sandstone layers against low-permeable clay-marl units is introduced to the base case model. The ~~arbitrary~~ fault is located in distances varying from 4 m to 118 m ~~from~~ of the borehole and resulted in a ~10% difference in the pressure field of the cases. ~~Modelling~~ Modelling the pressure and temperature distribution in the tilted reservoir with a borehole placed in the middle reveals that heat tends to accumulate updip while pressures ~~values~~ are ~~higher in the~~ downdip ~~side~~.

Keywords: HT-ATES, GMSH, Greater Geneva Basin, DeepStor, geological uncertainty, numerical ~~modelling~~modelling

1 Introduction

Aquifer Thermal Energy Storage (ATES) yields the highest storage capacities compared to other energy storage solutions (Fleuchaus et al., 2018). Based on the injection temperature and application, ATES falls into two categories: I) High-Temperature (>50 °C) Aquifer Thermal Energy Storage (HT-ATES; e.g., Wesselink et al. (2018)) and II) Low-Temperature Aquifer Thermal Energy Storage (LT-ATES; e.g., Réveillère et al. (2013)).

Seasonal storage constitutes a low risk in terms of time, budget and performance (Fleuchaus et al., 2020a). The typically applied "huffpush-puffpull" concept of HT-ATES foresees facilitates the horizontal transport of large volumes of fluid within an aquifer. Push-pull operation requires a single well for the injection and production. Hence, it is more efficient than the "flow-through" operation especially in the testing phase (Wang et al., 2020). HT-ATES provides a significant advantage in its reduced site dependence compared to conventional deep geothermal utilizationsHT-ATES offers the major advantage to be less site-dependent compared to conventional deep geothermal utilizations. It exploits suitable aquifers that can be encountered in the deeper subsurface of major populated urban areas (Schmidt et al., 2018; Mahon et al., 2022). Appropriate reservoir conditions for heat storage are widely distributed in the topmost uppermost 2 km of the Earth´s continental crust (Bloemendal et al., 2014; Gao et al., 2019; Dinkelman and van Bergen, 2022; Fleuchaus et al., 2020a; Pasquinelli et al., 2020). Suitable reservoirs for thermal energy storage can also even be found also inexist in thick successions of fractured rocks (e.g., Birdsell and Saar (2020)). Another advantage of HT-ATES is its minimal surface area requirement, making it an attractive option for densely populated urban areasAs another advantage, HT-ATES's requires small surface area comprising an asset in populated urban zones (Böhm and Lindorfer, 2019).

A successful design of aDevelopment of HT-ATES hinges depends on appropriate petrophysical properties of the deep aquifer that can be used as a reservoir. Such design requires conceptual geological and numerical models. Most HT-ATES studies on HT-ATES describe reservoir geometries as homogeneous kilometer-scale, box-shaped volumeskm large, box shaped volumes. The sensitivity of these volumes to relevant parameters (e.g., well configuration, transmissivity, flow rate, conductivity, …) has been extensively intensively studied (Stricker et al., 2020; Green et al., 2021; Mindel and Driesner, 2020; Fleuchaus et al., 2020a; Fleuchaus et al., 2020b). The conceptual designs of both, HT- and LT-ATES, typically apply box box-shaped reservoir simulations while disregarding ignoring natural geometries and impact of geological uncertainties.

Establishing HT-ATES in previously exploited oil fields leverages thebenefits from data and experiences gained from past exploration and production activitiesacquired during previous exploration and production. Some previously exploiteddepleted hydrocarbon reservoirs are re-used for natural gas storage to back up higher meet increased demand during winter season. Compared to CO_2 (Li et al., 2006) or H_2 (Muhammed et al., 2023) storage, In terms of heat storage, these depleted reservoirs have not yet been are yet less commonly used for heat. This scarcity of experience necessitates the development of numerical modelling approaches.used and this lack of experience requires the need for numerical modelling approaches.

Feldfunktion geändert
Feldfunktion geändert
Feldfunktion geändert
Feldfunktion geändert
Feldfunktion geändert
Feldfunktion geändert
Feldfunktion geändert
Feldfunktion geändert
Formatiert: Tiefgestellt
Feldfunktion geändert
Formatiert: Tiefgestellt
Feldfunktion geändert

Subsurface data inherently ~~inevitably~~ encompass varying ~~different levels~~ of uncertainty originating from measurement errors, biased extrapolations and interpretations, heterogeneities, and simplifications (Caers, 2011; Wellmann and Regenauer-Lieb, 2012; Wellmann et al., 2010; Wellmann and Caumon, 2018). In this study we focus on the impact of structural and geometrical uncertainties on pressure and temperature distribution and their spatio-temporal development in heat storage reservoirs during operation. These uncertainties comprise varying ~~topologies~~ morphologies of the reservoir roof and floor surfaces and sub-seismic faults that laterally delimit the reservoir, but cannot be predicted from surface measurements. These impacts are ~~commonly~~ often simplified or ignored due to the complexities involved in re-meshing~~due to complex re-meshing process~~ in numerical analyses. ~~Advancement in geological uncertainty studies are starting to be transferred into numerical simulations (Dashti et al., 2023).~~ Prognostic geological models cannot cope with the uncertainties of the subsurface. Uncertainty analysis ~~points to~~highlights the necessity of applying stochastic geological models rather than a deterministic geometrical representation. This study ~~extends~~ expands the application presented ~~by~~ in Dashti et al. (2023) by introducing an automated workflow that transfers stochastic structures from geological uncertainty models to a fast and reliable numerical meshing tool, enabling the quantification of relevant processes in HT-ATES.~~on an automated workflow to transfer stochastic structures from geological uncertainty models to a fast and reliable numerical meshing tool that allows the quantification of the relevant processes in HT-ATES.~~

In this study, two potential HT-ATES sites~~candidates for HT-ATES~~ in the vicinity of populated areas are evaluated: 1) the Greater Geneva Basin (GGB) next to Geneva (SW Switzerland) and 2) the designated DeepStor site, located at the ~~Campus~~ campus of Karlsruhe Institute of Technology (KIT; SW Germany). These two locations exhibit significant differences in reservoir geometry, lithology, petrophysical properties, and thicknesses for HT-ATES applications.~~These two locations differ strongly by their reservoir morphology, lithology, petrophysical properties, and thicknesses for HT-ATES.~~ To assess the impact of structural uncertainties on both the Geneva and DeepStor HT-ATES cases, we designed different scenarios.~~For both the Geneva and DeepStor HT-ATES cases we have investigated the impact of structural uncertainties, i.e. accuracy of geological data, on them by designing different scenarios.~~ Quantification of the uncertainty included thickness and ~~topology~~ geometry variations by adapting a fast, specific meshing workflow. Different scenarios with identical material properties but variating meshes (geologies) are run for each HT-ATES case. The meshing routine generates surfaces from point clouds ~~in order~~ to create arbitrary shaped volumes ~~with topologies derived from 3D seismic analyses~~. The meshing procedure allows to establish various stochastic numerical models that account for the resolution of the data and even can include for additional fault zones. Consequently~~This way~~, meshing routines represent the basis for advanced thermohydraulic analyses from arbitrarily inserted faults into the model.

Feldfunktion geändert

Feldfunktion geändert

2 Uncertainty and Numerical model developments

2.1 Greater Geneva Basin

~~A proposed HT-ATES~~The HT-ATES system proposed for the outskirts of Geneva is situated within the GGB and is designed to store the excess thermal energy, up to 35 GWh, from a nearby power plant ~~system in the outskirt of Geneva is located in the Greater Geneva Basin (GGB) and is supposed to be charged by surplus 35 GWh from a nearby power plant~~ (Collignon et al., 2020). For details on the geology of the GGB, refer to ~~see~~ Kuhlemann and Kempf (2002). Two formations are recognized as potential heat storage reservoirs: thick Upper Jurassic Malm limestones and thin sand-rich layers in the Cenozoic Molasse sediments (Chelle-Michou et al., 2017). The geothermal gradient for the GGB ~~comprises~~ is equal to 25-30 K/km (Rybach, 1992; Chelle-Michou et al., 2017). The 2530 m deep geothermal well (Thonex-01) intersected >900 m thick Malm limestones and marl succession with a bottom hole temperature of 88 °C and low flow rates of <0.5 l/s (Guglielmetti et al., 2022). The geothermal gradient is not very promising for geothermal heat production from the reservoir, but heat storage can efficiently support the higher heat demand during the winter season.

Collignon et al. (2020) conducted ~~published~~ a local parametric sensitivity analysis on Molasse and Malm limestone reservoirs of the HT-ATES. The proposed target Malm limestones are considered to consist of patch reefs with high porosities (Chevalier et al., 2010; Rybach, 1992). In their scope study, Collignon et al. (2020) assumed a ~~box~~ box-shaped reservoir with flat top and bottom surfaces at the depths of -1100 and -1200 m, respectively. Our study simulates the pressure and temperature fields in the geometrically different Malm reservoirs while the material properties are fixed and identical. We investigate the impact of the geological uncertainty caused by the carbonate reservoir ~~on pressure and temperature~~. Such ~~uncertainty~~ uncertainties typically ~~originate~~ stem from the exploration of a reservoir structure that is based on earlier seismic data acquisition (Feng et al., 2021; Faleide et al., 2021). The sources of error comprise data acquisition, preprocessing, stacking, migration, availability of borehole data for depth calibration, quality of velocity models for time-depth conversion, ambient noise level (Bond, 2015; Thore et al., 2002).

To perturb the geological model, a randomized noise is superimposed ~~superposed~~ on the ~~upper~~ top and ~~lower~~ bottom surfaces of the reservoir layer ~~that are assumed to be inverted from 3D seismic data~~. This noise is introduced randomly to avoid any bias. This study follows the work applied on a generic box with flat surfaces in Collignon et al. (2020); consequently, the introduced uncertainty also remains generic. For the top surface, a range of ± ~~8~~10 m arbitrary noise is imposed on the primary flat plane. For the bottom surface, the range of perturbation is increased to ± ~~10~~15 m due to the decrease in the quality of seismic data with depth.– The availability of the borehole data allowed for well-to-seismic tie which increases the accuracy. In the geological model, it is assumed that at intersections of the wells with the top (-1100 m) and bottom (-1200 m) surfaces of the reservoir, the depth value is a certain data. A simplified 2D schematic is presented in Figure 1-a to visualize the process of assigning generic uncertainty to the depth data of the GGB. As shown in the figure, the base case assumes the simplest geometry, and all scenarios must pass through the four certain points.

Feldfunktion geändert
Feldfunktion geändert
Feldfunktion geändert
Feldfunktion geändert
Feldfunktion geändert
Feldfunktion geändert
Feldfunktion geändert
Feldfunktion geändert
Feldfunktion geändert
Feldfunktion geändert
Formatiert: Schriftart: 10 Pt., Nicht Fett

~~A surface can be considered as discrete points in x, y and z coordinates of a 3D space.~~ For the Malm limestone reservoir, a grid of discrete points in x, y and z coordinates of a 3D space (representing surfaces) is generated. The regular grid consists of 41×26 nodes in x and y directions, respectively with a fixed 20 m distance. ~~The~~ perturbed model is a purely generic example where at each grid point the random noise is added to its vertical coordinate like the 2D example in Figure 1-a. In realistic cases, geological surfaces may be subjected to other sources of uncertainty. For instance, a function could be defined to establish a direct relationship between the noise value and the distance from the wells, addressing spatial correlation. However, this approach could lead to generating a reservoir with concave or convex surfaces, while meshing highly complex surfaces is one of the contributions of this study. ~~The base case of this study corresponds to the reference model of Colligon et al. (2020). Figure 1~~Figure 1-b presents a scenario with two perturbed surfaces of the Malm limestone layer. ~~T~~Figure 1-a shows ~~h~~e roughness and irregularity of ~~t~~he ~~s~~urfaces ~~may be visualized in figure~~ ~~T~~he ~~p~~erturbed ~~g~~rid ~~m~~ainly ~~p~~rovides ~~t~~he ~~f~~lexibility ~~o~~f ~~c~~hanging ~~p~~erturbation ~~v~~alues ~~f~~or ~~e~~ach ~~n~~ode ~~i~~ndividually ~~f~~or ~~a~~ ~~r~~ealistic ~~s~~cenario. ~~T~~he ~~v~~alues ~~a~~dded ~~t~~o ~~t~~he ~~g~~rid ~~n~~odes ~~(~~Figure 1-b~~)~~ include ~~s~~mooth ~~r~~eservoir caprock as lower, middle and upper units, respectively.

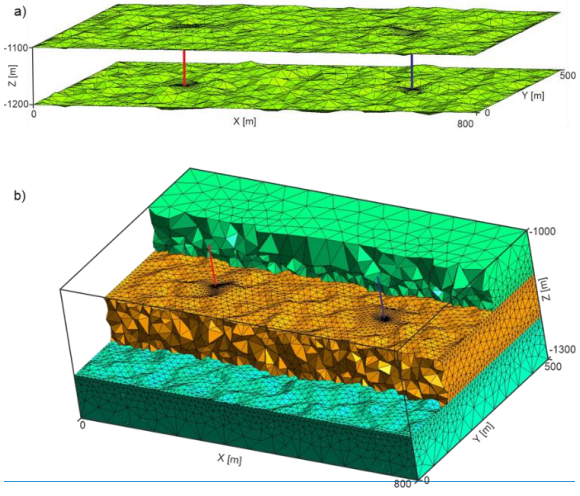

Feldfunktion geändert

Formatiert: Schriftart: 10 Pt., Nicht Fett

Feldfunktion geändert

Feldfunktion geändert

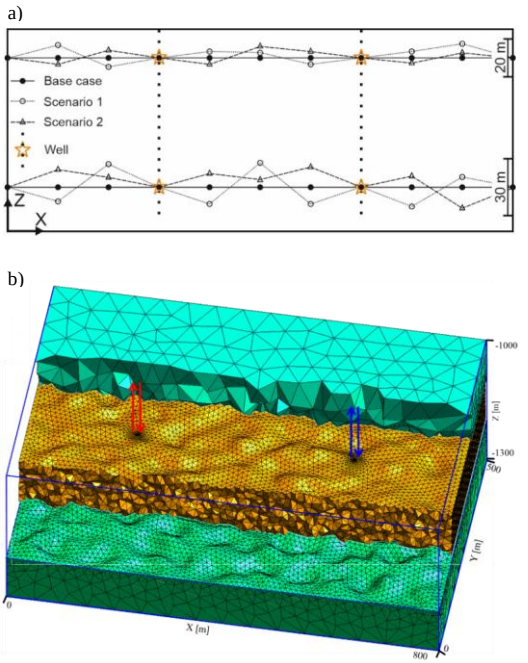

Figure 1: **a) The solid line passing through black dots represent the base case. In each of the three scenarios the geometry of the reservoir is different but all the lines pass through the orange star which highlights the contact point of the wells and reservoir. b) ~~a) Randomly perturbed top and bottom surfaces of the Malm limestone reservoir. b)~~ The ~~whole~~ entire discretized model of a perturbed scenario. The reservoir layer in the middle is sandwiched by the basement and caprock units. Red ~~line~~ arrows represent~~s~~ the injection and production operation in the ~~warm~~ hot well whereas the cold well is shown with the blue ~~line~~ arrows in both subplots.**

2.2 DeepStor

The proposed DeepStor site is located in the Cenozoic sediments of the Upper Rhine Graben (URG) and ~~intended~~ aims to use an abandoned and depleted oil field for thermal storage in the sand layers of the Oligocene Meletta beds. For details on the geology and stratigraphy of the URG, ~~see~~ refer to Grimmer et al. (2017), Dèzes et al. (2004) and Schumacher (2002) and references therein. Figure 2~~Figure 2~~ highlights the abundance of ~~the~~ normal faults in the URG that – if suitably oriented in the stress field – facilitate convective fluid flow in fractured Permo-Mesozoic and crystalline basement rocks. Convection in fractured Permo-Mesozoic rocks creates~~The convective regime builds~~ positive thermal anomalies in the Cenozoic graben filling ~~sediments~~ generating locally ~~with~~ geothermal

Feldfunktion geändert
Feldfunktion geändert
Feldfunktion geändert
Formatiert: Schriftart: 10 Pt., Nicht Fett

gradients of up to 100 K/km (Agemar et al., 2012; Baillieux et al., 2013; Pribnow and Schellschmidt, 2000). DeepStor designated HT-ATES ~~targets~~ aims to utilize the Oligocene Meletta sandstones that were exploited for oil ~~production~~ from 1957 to 1986 (Reinhold et al., 2016) in the footwall of the sealing Leopoldshafen fault where oil and some gas accumulated updip (Wirth, 1962; Böcker et al., 2017).

The DeepStor model in this study encompasses ~~comprises~~ a volume ~~of~~ with 1000×1000 m^2 area and 250 m ~~thickness~~ height (see Figure 3~~Figure 3~~-a with the sand layers of the Meletta beds). Due to the inherent ~~overall~~ uncertainty~~ies~~, sub-seismic faults characterized by offsets <20 m cannot be accurately identified using either 3D seismic or borehole data. These faults can laterally delimit thin reservoir layers and [illegible] (Lüschen et al., 2022). To the best of our knowledge, mathematical models have been developed to characterize these faults due to their abundance and importance (Gong et al., [illegible] seismic faults are expected to be present~~are expected~~, ~~but~~ their location in the subsurface remains largely unknown.

~~In order t~~To evaluate the impact of sub-seismic faults on HT-ATES operation, an arbitrary N-S-striking fault is introduced in different parts of the basic geological model. The ~~S~~strike of this ~~arbitrary~~ fault is parallel with Stutensee and Leopoldshafen faults (Figure 2~~Figure 2~~). The uniform dip-slip displacement of the introduced sub-seismic fault exceeds the thickness of the reservoir. This pessimistic assumption enables the prediction of the worst-case scenarios for the storage in which a sealing fault completely blocks the thin reservoir. If the offset is reduced and some contacts between the reservoir on either side of the fault are permitted, the effect of the fault diminishes. Our modelling results are also applicable for faults with larger dip-slip [illegible] (Figure 2). Timing with real storage cases where a test well allows for optimal design. Data from this well is subsequently processed to establish a potential relationship between measured pressure values and the location of a sealing fault. This study evaluates the impact on reservoir temperature and pressure through thermohydraulic simulations for 16 fault locations. The borehole and fault are modelled as vertical lines and planes, respectively. ~~This way, the DeepStor model is more similar to real storage cases where a test well allows for an optimum design. The data from this well is later on processed to establish a possible relation between measured pressure values and location of a sealing fault. This way, the DeepStor model is more similar to real storage cases where a test well allows for an optimum design. This test well is supposed to act as the warm well in the future. The fault has moved 16 times around the well in order to quantify its impact on temperature and pressure in the reservoir through thermohydraulic simulations. The borehole and fault are modelled as vertical lines and planes, respectively.~~ In total 17 scenarios are considered, which can be categorized into three groups based on the subsurface geology (mesh) as:

- Fourteen scenarios with a fault varying from 4 m to 112 m distances east of the well
- Two scenarios with a fault in the west of the well at 8 and 48 m distances
- One fault-free base case

Figure 3~~Figure 3~~-b represents a scenario with a possible location of the arbitrary fault at 98 m distance in the east of the well.

Feldfunktion geändert

Feldfunktion geändert

Formatiert: Schriftart: 10 Pt., Nicht Fett

Feldfunktion geändert

Feldfunktion geändert

Feldfunktion geändert

Formatiert: Schriftart: 10 Pt., Nicht Fett

Feldfunktion geändert

Formatiert: Schriftart: 10 Pt., Nicht Fett

Feldfunktion geändert

Formatiert: Schriftart: 10 Pt., Nicht Fett

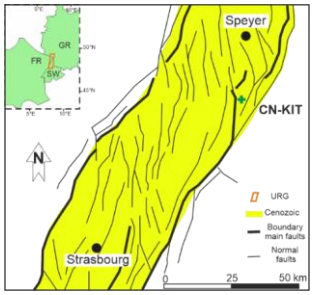

Figure 2: A tectonic overview of the URG and its surrounding area. The green plus symbol indicates the proposed location for HT-ATES in the north of Karlsruhe. Bold lines mark major faults of the rift boundary fault system. DeepStor site is located between Leopoldshafen (in west) and Stutensee (in east) normal faults (modified from Grimmer et al. (2017)).

Feldfunktion geändert

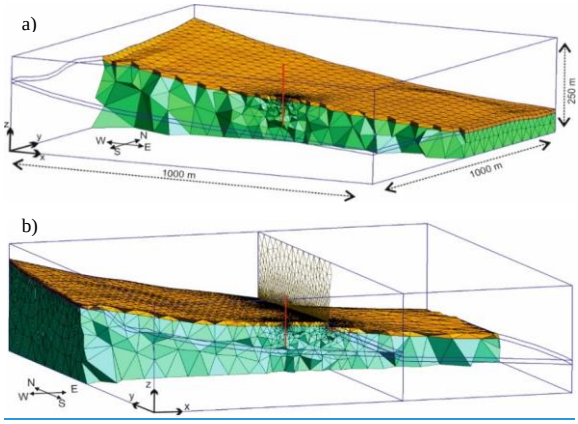

Figure 3: a) A section across the permeable reservoir layer (orange) and ~~impermeable host rocks~~basement (green) of the DeepStor base case. Impermeable clay caprock is not shown to have a better view on the spatially discretized model and topology of the thin reservoir layer. b) A sealing fault is introduced in the model. Dimension of the faulted model remains the same as the base case represented in subplot a (1000×1000×250). Fault surface of this example is located 98 m east of the well. In both subplots the well location is shown via a red line.

A simplified example in Figure 4 illustrates how the fault embedding is achieved in the DeepStor model. Figure 4-a depicts two surfaces with different colours representing the simplified top and bottom surfaces of the DeepStor reservoir in the base case. For better visualization, surfaces are divided into patches and points are labelled with numbers from 1 to 36. In reality a single surface is generated that fits the grid point of the upper surface (18 black dots) and the same for the lower surface (18

Formatiert: Schriftart: 10 Pt., Nicht Fett
Formatiert: Schriftart: 10 Pt., Nicht Fett
Feldfunktion geändert
Feldfunktion geändert
Formatiert: Schriftart: 10 Pt., Nicht Fett

black triangles) (Figure 4-a). The fault then displaces the reservoir layer as shown in Figure 4-b. The fault's outline in the model is represented by thick red lines passing through points 10, 11, and 12 on the top surface and points 28, 29, and 30 on the bottom surface. The workflow is designed to incorporate N-S striking faults that pass through grid points. Therefore, the grid resolution in the x-direction (14 m in the existing DeepStor model) determines the fault's position. The borehole in the simplified example indicates the certain depths of the top and bottom surfaces in the model. In the faulted example, the top surface will be divided into two splits: the first split including point numbers from 1 to 12 (left hand side of the fault) and the second one with point numbers 10 to 18 (right hand side of the fault). The left hand side split of the fault does not move and only the right one is displaced downward by the amount of the offset, acting as the hanging wall and juxtaposing the reservoir against the impermeable basement. This approach is used in this example because the borehole is located within the left hand side split. For each split, an extra set of points are also considered to ensure that the split is properly intersected by the fault plane. In the first split of the top surface, point numbers 13, 14 and 15 are added. One single surface fitting to point numbers 1 to 15 will be generated for this split. Two hashed patches in Figure 4-b show how the extra points are allowing the first split of the top surface to extend toward the fault plane. For the second split of the top surface, points 7, 8 and 9 are additionally included. The second split of the top surface passes through 12 black dots numbered from 7 to 18. This surface generation process is repeated for the bottom surface, whose points are represented by black triangles. Finally, the fault plane will also be generated and intersects each split of the top and bottom surfaces. All the hashed patches in Figure 4-b show how the extra points will allow the splits to pass through the fault plane. These extra patches and their corresponding points and lines can be deleted after generating the correct geometry. The explained process allows displacing the grid points of the DeepStor base case or GGB. In the base case (Figure 4-a) 36 grid points are required to create two separate surfaces, namely the top and bottom of the reservoir, while in the faulted case (Figure 4-b) the number of points increases to 54. All the explained steps are implemented and elaborated in an example (see Code and data availability section).

Formatiert: Schriftart: 10 Pt., Nicht Fett

Formatiert: Schriftart: 10 Pt., Nicht Fett

Formatiert: Schriftart: 10 Pt., Nicht Fett

Formatiert: Schriftart: 10 Pt., Nicht Fett

Feldfunktion geändert

Formatiert: Schriftart: 10 Pt., Nicht Fett

Formatiert: Schriftart: 10 Pt., Nicht Fett

Feldfunktion geändert

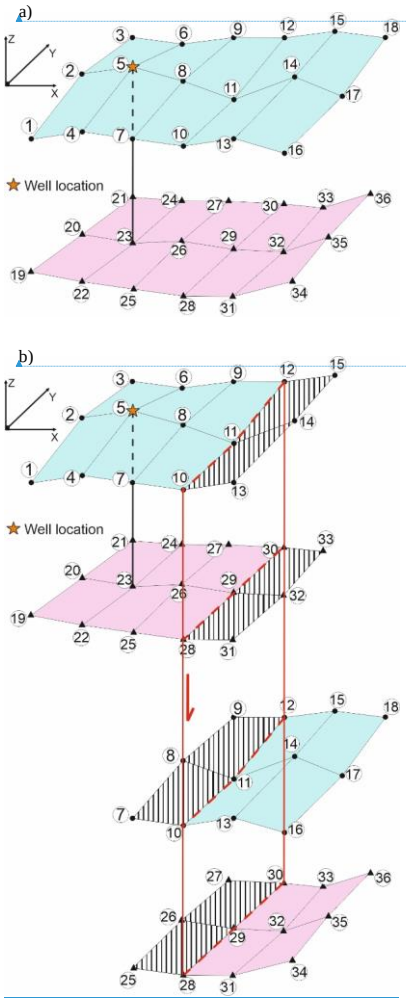

Formatiert: Schriftart: 9 Pt.

Formatiert: Schriftart: 9 Pt.

Figure 4: a) Top and bottom surfaces of the simplified reservoir layer are represented via blue and pink patched surfaces, respectively. Black dots represent the point grid of the top surface while the bottom surface passes through the black triangles. The borehole location and trajectory are shown via an orange star and a line, respectively. b) A normal fault with an arbitrary offset is displacing the hanging wall (right hand side splits) down. Hashed patches are the extra ones added to each split.

2.3 Tool developments based on GMSH

The open source finite element mesh generator GMSH (Geuzaine and Remacle, 2009) is used to generate the required high quality spatial discretization. GMSH recently gained the ability to create geometrical surfaces passing through arbitrary sets of points and to combine these surfaces with other geometrical entities (curves, surfaces or volumes) through Boolean operations thanks to the built-in OpenCASCADE geometry kernel (Open CASCADE Technology). The new features linked to B-Spline surface interpolation and non-manifold meshing are available in the latest stable version of GMSH (v. 4.11). This allows to preserve the geological topology of the layers and enables the generation of high quality, adapted finite element meshes for complex geometries like modified Malm limestone reservoir surfaces (Figure 1~~Figure 1~~) or thin, tilted Meletta beds (Figure 3~~Figure 3~~). ~~While~~ the model of Dashti et al. (2023) lacks complicated geometries, the recently added functionality of GMSH is tested in this study by implementing complex ~~topologies~~geometries. The overall workflow for the spatial discretization is based on the following steps that are implemented in ~~a template~~fully elaborated scripts using Python API of GMSH (see ~~code~~ Code and data availability section):

- The global outline of the domain of study is defined by adding a single (solid) volume – usually a parallelepiped;
- Geological layers are defined by fitting, through numerical optimization, a B-Spline surface going through each set of data points defining a geological interface. The point cloud can come from any modelling tool and the only requirement is that they should make a regular grid. Simplified schematics like Figure 4 show how the input point cloud can look like. GMSH only requires the x, y and z values of each point. Default parameters for the B-Spline degree and the tolerances for the fitting ensure a smooth surface with reasonable local curvature changes;
- Sources and wells (or other zero- or one-dimensional features) are defined as additional points and curves in the model;
- All the geometrical entities are intersected globally in order to produce a conforming boundary representation of the complete model, possibly with non-manifold features (points and curves “embedded” in surfaces and/or volumes);
- ~~The link between geometrical entities and physical properties is established using representative points;~~

The global unstructured mesh is then generated automatically. The mesh is made of tetrahedra inside volumes, triangles on the interfaces, lines on the wells and points on the sources. This mesh is conforming, i.e. the elements are arranged in such a way that if two of them intersect, they do so along a face, an edge or a node, and never otherwise. It is necessary to first generate the desired number of scenarios for uncertainty analysis and later on one single block of code in Python will yield the same number of meshes.

In the GGB cases and also the base case of the DeepStor, only two surfaces representing the top and bottom of the reservoir are generated in the mesh. In the faulted cases of the DeepStor (Figure 4-b), the grid points making the top and bottom surfaces of the reservoir are discontinuous due to the presence of the fault. Therefore, GMSH should make four different

Feldfunktion geändert
Formatiert: Schriftart: 10 Pt., Nicht Fett
Formatiert: Schriftart: 10 Pt., Nicht Fett
Feldfunktion geändert
Feldfunktion geändert
Feldfunktion geändert
Formatiert: Schriftart: 10 Pt., Nicht Fett
Feldfunktion geändert
Formatiert: Schriftart: 10 Pt., Nicht Fett

surfaces to reconstruct the faulted scenarios. It also generates a plane surface as the fault. As visualized in Figure 4-b, each split is extended to intersect the fault surface, resulting in some additional small surfaces. These extra parts can be removed in GMSH before meshing. Comprehensive Jupyter notebooks are provided (see the Code and data availability section) to detail each step of the meshing process for both the DeepStor and GGB cases.

Multi-level mesh refinement is implemented in both models using various functions available in GMSH. ~~A multi-level mesh refinement in both models is carried out through several available functions in GMSH.~~ In the GGB case, Distance and Threshold fields enable a gradual mesh size increase from 2 m to 75 m, starting from the boreholes and extending towards the model boundaries~~In the case of GGB, Distance and Threshold fields allowed for a gradual mesh size increase of 2 m to 75 m from the boreholes toward the boundaries of the model~~. Additionally, the mesh size is set to 15 m near the Malm top and bottom surfaces and gradually increases to 75 m~~In the adjacency of the Malm's contacts also mesh size was set to be 15 m while it increases up to 75 m~~. On average, GGB meshes contain approximately 35'000 nodes and 210'000 elements. The average is presented due to the scenario-specific variations in the mesh caused by geometrical differences. The fast and automated workflow facilitates the generation of meshes for complex geological models, such as the perturbed GGB scenarios, within 80 seconds on a Core i7 laptop. Notably, the running time encompasses the entire process from importing data into GMSH to exporting a refined conforming mesh.

DeepStor employs the same refinement strategies but with different mesh sizes. The minimum mesh size is set to 0.5 m near the single borehole and gradually increases to 125 m. The model also includes a large fault plane, increasing the mesh complexity. Distance and Threshold fields are introduced for the fault plane, forcing the mesh size to be 3 m in the immediate vicinity of the fault. The DeepStor base case contains 9'026 nodes and 62'317 elements. The mesh is generated in 45 seconds for this fault-free case. For the 16 scenarios with the sub-seismic fault, the number of nodes and elements increases to 37'000 and 250'000, respectively. To achieve the specified mesh sizes in both GGB and DeepStor cases, a mesh sensitivity analysis was conducted to ensure the independence of simulation results (temperature and pressure fields) from the mesh size.~~In total, GGB meshes have an average of 35'000 nodes and 210'000 elements. The average is presented here because from scenario to scenario, the mesh is different due to topological variations. The fast and automated workflow allows for generating a mesh in a complicated geological model like the perturbed scenarios of GGB in 80 sec running on a Core i7 laptop. Noteworthy, running time includes the whole process from importing the data into GMSH up to exporting a refined conforming mesh. For DeepStor also the same refinement strategies but with different mesh sizes are used. Minimum mesh size is set to be 0.5 m close to the single borehole while it gradually increases to 125 m. The model contains also a large fault plane making the mesh more complex. Distance and Threshold fields are introduced for the fault plane forcing the mesh size to be 3 m in the immediate vicinity of the fault. The base case of the DeepStor does not include the fault plane and the number of nodes and elements are 9'026 and 62'317, respectively. In the base case of DeepStor the mesh is generated in~~

2.4 Numerical modelling

The open source finite element application TIGER (Thermo-Hydro-Chemical sImulator for Geoscience Research) (Gholami Korzani et al., 2020) is used to simulate the heat storage processes for GGB and DeepStor cases. TIGER is developed on top of the MOOSE (Multiphysics Object-Oriented Simulation Environment) framework. As a general-purpose PDE environment, ~~The~~ the MOOSE framework ~~-~~is fully coupled and encompasses a wide variety of completely implicit solvers (Lindsay et al., 2022; Gaston et al., 2009). It inherits functionalities ~~of~~ from PETSc ~~(~~which is a suite of data structures and routines applied for ~~the~~ scalable parallel solution~~)~~ and libMesh ~~libraries~~that allows for generating and also reading spatial discretization. In our study the coupled thermal and hydraulic kernels of ~~the~~ TIGER are deployed to obtain the evolution of temperature and pressure~~-~~. In TIGER, the mass transport equation (given by mass balance along with the Darcy velocity) is used to simulate the hydraulic behaviour of the system. For the heat transport, TIGER uses the advection-diffusion equation (Gholami Korzani et al., 2020). ~~-~~TIGER simplifies the meshing by enabling a mixed-dimensional problem formulation. In GMSH, the connection of lower and higher dimensional elements is implemented straightforwardly, facilitating quick implementation~~so straightforward that can be achieved quickly~~. Therefore, we considered the wells and faults in the mesh as 1D lines and 2D surfaces, respectively.

Used thermal and petrophysical data for simulation of both cases are directly ~~coming~~ obtained from the published models. Table 1~~Table 1~~ contains the values selected for required parameters in our simulations. Considering homogenous petrophysical properties for patch reefs is highly idealized, but we adhere to the available published data in this instance. Otherwise, a wide range of uncertainty/heterogeneity can be considered for each parameter. Collignon et al. (2020) used MATLAB Reservoir Simulation Toolbox to simulate the thermohydraulic processes. ~~but i~~In this study, ~~TIGER is used for~~ simulation ~~and~~ results (heat plume propagation and recovery) are compared and benchmarked against ~~based on~~ their work.

The GGB model includes a doublet system simulated over a 10-year time frame~~in a 10-year time scheme~~. The l~~L~~oading, unloading and resting phases of the model follow the strategy introduced by Collignon et al. (2020). Each annual cycle comprises ~~includes~~ four months of loading, two months of rest, four months of unloading, and two months of rest. The loading phase corresponds to the injection of hot water via the ~~warm~~ hot well when the cold well is ~~under~~ in production. Temperatures for hot and cold fluid injection are set to be 90 °C and 39 °C, respectively. Both wells have a fixed flow rate of 10 l/s but in different directions. The time stepping for 10 years of simulation is divided into 10 loading, 10 unloading and 20 rest phases. The piecewise linear function of MOOSE is used to increase the time steps in each phase to have a more efficient numerical convergence. During the first cycle (four months of injecting hot fluid into the hot well and producing from the cold well), the time step size increases from one hour to 10 days. Subsequently, the time step size decreases to one hour at the beginning of the rest cycle (two months) and gradually increases to 20 days at the end. At the start of the next four-month cycle (producing from the hot well and injecting cold fluid into the cold well), the time step size is forced to be one hour and increases to 10 days. For GGB, the simulation runtime is approximately 3 hours on 12 cores of a high-

Feldfunktion geändert

Feldfunktion geändert

Feldfunktion geändert

Formatiert: Schriftart: 10 Pt., Nicht Fett

Feldfunktion geändert

Feldfunktion geändert

Stricker et al. (2020) introduced properties of the reservoir for DeepStor in a generic model and we used the data of their reference case (Table 1~~Table 1~~). In our simulations the geology and consequently the mesh is the major difference to the model of Stricker et al. (2020) while petrophysical parameters, parameterization scheme remain the same. ~~The simulation time is set to 10 years.~~ Rather than the doublet model described by Stricker et al. (2020), a single "~~huff~~push-~~puff~~pull" well is demonstrated in our study. Herein we ~~are focusing~~focus on the thermohydraulic impacts in the near field of a single well and our model works with a single well scenario. The simulation time is set to 10 years. Hot fluid with a temperature of the hot fluid with 140 °C temperature is injected in a six-month period, followed by six months of production operation and during the subsequent six months the well produces the previously injected fluid at the same. The flow rate is fixed to be 42 kg/s in both the injection and production phases. ~~Heat exchange between the hydraulic partitions of the aquifer and the overlying and underlying clay layers is neglected.~~ The density of water is not dynamic and is computed at the reference temperature of the whole simulation time. Time steps increase from 10 minutes to 10 days in each cycle. Time steps at the start point of each cycle are considered to be shorter in the DeepStor ~~model~~ simulations compared to GGB due to the lower thickness of the reservoir and higher complexity of the model. Almost 74'000 degrees of freedom in the faulted scenarios demands for an average of 4 hours computation time on 12 cores of a HPC cluster with 62 gigabyte of RAM. Simulations in the faulted scenarios of the DeepStor are computationally more demanding compared to GGB due to the complexity of the model.

For both the GGB and DeepStor cases, similar strategies applied for defining boundary and initial conditions. After running a ~~steady~~ steady-state thermohydraulic simulation for each scenario, the results have been applied as the initial condition for that specific case. In other words, 17 ~~steady~~ steady-state models are calculated for the DeepStor and each one is used as the initial condition of the transient simulation. In both the steady state and transient simulations, ~~Two~~two Dirichlet ~~-~~boundary conditions are also applied for the temperature variable at the top and bottom surfaces of each model. By introducing a function that ~~representing~~ represents the temperature gradient, MOOSE allows for assigning the correct temperature values to the ~~top and bottom surfaces of the~~ model. The depth-dependent temperature function~~The function~~ is mentioned in the following:

$$T(z) = T_{surface} + z \times GT, \quad (1)$$

where z denotes the depth (in m) and GT the geothermal gradient (in K/km). In the case of pressure, one Dirichlet boundary condition is defined on the bottom surface of the model based on the following function for both the steady state and transient simulations (assuming hydrostatic equilibrium):

$$P(z) = (z - WT) \times \rho \times g, \quad (2)$$

where WT represents the water table, ρ is the density (in kg/m^3) and g is the gravitational acceleration (set as 9.81 m/s^2).

Neither temperature nor pressure BCs are set on the side faces, hence they follow the gradient. All the faces of the models are considered as open to flow. The sizes of the models are also big enough to avoid any interaction between the pressure and temperature values of the boundaries and injection-production operation.

Feldfunktion geändert

Formatiert: Schriftart: 10 Pt., Nicht Fett

Feldfunktion geändert

Table 1: Parameters selected as inputs ~~from~~ for the numerical simulations of two case studies.

Parameter		Case studies	
		GGB (Collignon et al., 2020)	DeepStor (Stricker et al., 2020)
Reservoir	Thickness [m]	~100	10
	Permeability [m^2]	9.8×10^{-15}	6.6×10^{-14}
	Porosity [-]	0.15	0.15
	Thermal conductivity [W/mK]	1.8	2.5
Caprock and basement	Thickness [m]	~100	~100
	Permeability [m^2]	9.8×10^{-19}	10^{-18}
	Porosity [-]	0.05	0.15
	Thermal conductivity [W/mK]	1.4	1.4
Flow rate [l/s]		10	2
Geothermal gradient [K/km]		26	50
Water table [m]		10	10

Feldfunktion geändert

Feldfunktion geändert

3 Results

3.1 GGB

The upper and lower contacts of the reservoir are perturbed to investigate their possible effect/s on the heat and pressure distributions in the HT-ATES. The ~~H~~heat recovery of the system has remained unaffected~~not been affected~~ due to its dependence on local temperature values. Despite changing the ~~topology~~ geometry of the reservoir, propagation of the heat also ~~looks~~ appears the same for the three presented scenarios in Figure 5~~Figure 4~~. Temperature values of the highlighted traces in Figure 5~~Figure 4~~ are extracted to visualize the heat plume propagation. The uppermost scenario in Figure 5~~Figure 4~~ is the base case (a ~~box~~ box-shaped reservoir with flat planes) while the two next ones are named as scenario~~s~~ 1 and 2 in Figure 6~~Figure 5~~. Even after 10 years the heat is still locally propagated around the ~~warm~~ hot well for the base case and the other two perturbed scenarios (Figure 6~~Figure 5~~). The ~~O~~overlap of all three curves confirms the independence of the temperature field from introduced ~~topological~~ geometrical perturbation of the thick reservoir layer. ~~Heat plumes (Figure 4) and the curves (Figure 5) are slightly asymmetric due to the effect of the . During the injection of hot fluid in warm well, cold well is in production phase that pulls the hot fluid from the warm well toward itself.~~

Formatiert: Schriftart: 10 Pt., Nicht Fett

Formatiert: Schriftart: 10 Pt., Nicht Fett

Formatiert: Schriftart: 10 Pt., Nicht Fett

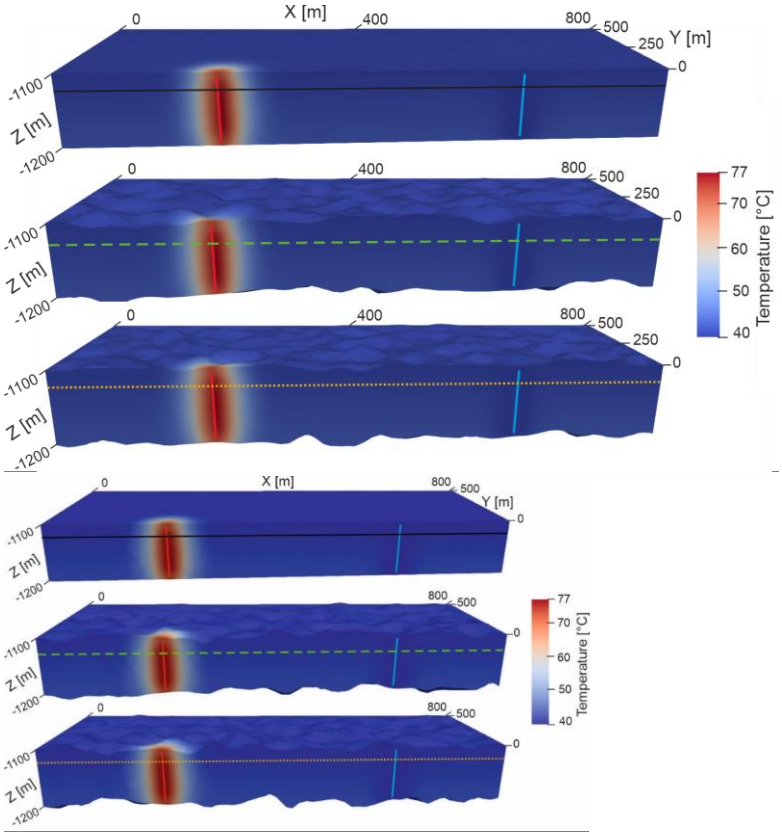

Figure 5: Heat distribution after 10 years of storage in the Malm limestone reservoir of the GBB. Red and blue lines represent hot and cold wells, respectively. The upper scenario with a uniform box-shaped reservoir is considered as the base case while contacts of the reservoir in the middle and lower scenarios are perturbed and irregular. Solid black, dashed green and dotted orange traces are used in Figure 6 for plotting the temperature values.

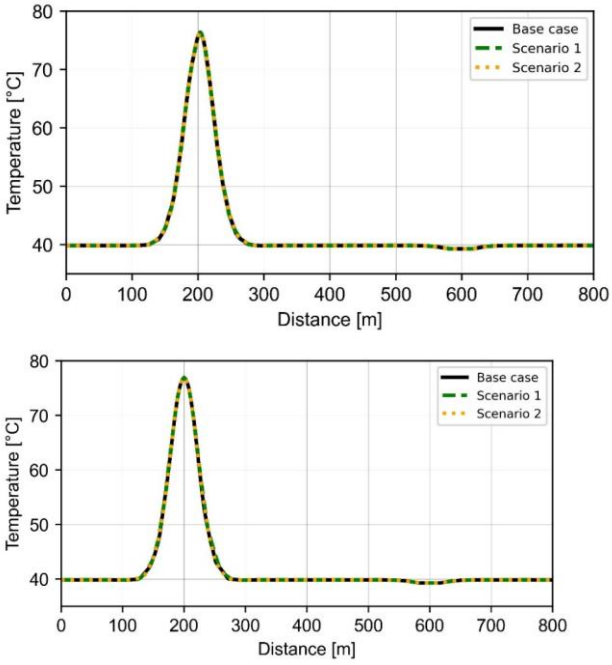

Figure 65: Temperature distribution curves of the values coming from the base case and two perturbed scenarios after 10 years of injection and production for the GGB. ~~Warm~~ Hot and cold wells are located at 200 m and 600 m points of the x axis. To find the location of the plotted trace~~s~~, refer to Figure 5~~Figure 4~~. ~~Similar to t~~The ~~models'~~ extension of the model in x direction ~~x axis (i.e.~~ Distance~~)~~ ~~(in m)~~ ranges from 0 m to 800 m.

3.2 DeepStor

For HT-ATES infrastructure, the ~~real~~ complex underground ~~topology~~ geometry of the target storage reservoir (sand layers in Meletta beds) is simulated. Despite incorporating the reservoir's real geology into this study~~In spite of including the real geology of the reservoir in this study~~, both the recovery and heat plume radius of the base case are similar to what is presented by Stricker et al. (2020) for their reference case. The recovery rate is calculated as the ratio between extracted and injected thermal energy at the top of the well's openhole section. Therefore, this parameter only covers the data from one single point of the 3D model and is unable see the difference between complex and simple reservoir structural models. ~~Figure 6 shows a recovery of 67 and 82 % when the reservoir is assumed to be a homogeneous layer cake. The recovery rate of the 17 simulated cases is negligible (~2 %).~~ Cases with the highest difference~~, i.e.~~ extremes, are plotted in Figure 7~~Figure 6~~ to keep the plot

Feldfunktion geändert

readable. The recovery difference between scenarios increases over time, as evidenced by the divergence of the three recovery curves. Meanwhile, the recovery difference of scenarios increases throughout the recovery curves converging. Despite the negligible difference, the case where the fault is located 48 m in the west of the well has the best performance while the case with a fault in 4 m distance in the east shows is the worst. For the best recovery, the reason is linked to the total volume of the reservoir and upward movement of the low-density hot fluid. The reservoir is tilted and hot fluids move updip due to the density effect. A sealing fault in 48 m distance from the injection point will keep the hot fluid within the confined reservoir. The reason behind the worst recovery is that the arbitrary fault affects the heat plume and results in heat loss.

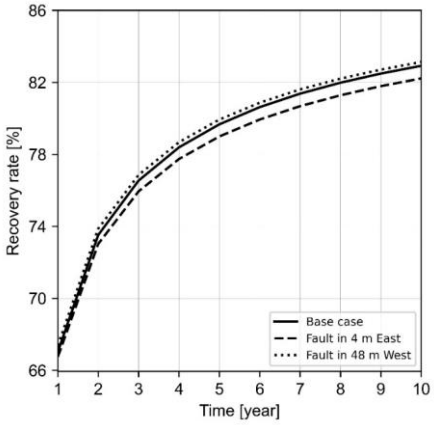

Figure 76: Heat recovery in three scenarios of the DeepStor model. Only two extremes and the base case are plotted to keep the plot more readable.

Figure 8Figure 7 shows the heat accumulation in four distinct different simulated scenarios. In the base case (Figure 8Figure 7-a), the size radius and temperature of the heat plume confirms corroborate the results of Stricker et al. (2020). The heat plume extends approximately about 45 m in x and y directions. The primary distinction is that the heat plume's slope aligns with the tilted reservoir in this instance. The only difference is that here the slope of the plume follows the tilted reservoir. The ~~a~~ gh between the total ~~add~~ wh and the heat plume in Figur Figure 7 indicates 5 that in Fa ~~a~~ ~~o~~ ~~i~~ ~~e~~ ~~d~~ ~~f~~ ~~h~~ ~~e~~ ~~h~~ ~~a~~ ~~l~~ ~~y~~ ~~d~~ ~~r~~ ~~a~~ ~~g~~ ~~j~~ ~~y~~ ~~k~~ ~~y~~ ~~a~~ ~~y~~ ~~f~~ ~~a~~ ~~l~~ ~~l~~ ~~a~~ ~~p~~ ~~l~~ ~~h~~ ~~f~~ ~~a~~ ~~m~~ ~~e~~ ~~S~~ ~~t~~ ~~a~~ ~~a~~ ~~f~~ ~~o~~ ~~l~~ ~~h~~ ~~a~~ ~~h~~ ~~a~~ ~~n~~ ~~a~~ ~~p~~ ~~f~~ ~~o~~ ~~n~~ ~~a~~ ~~e~~ ~~h~~ ~~y~~ ~~a~~ ~~i~~ ~~n~~ ~~O~~ ~~y~~ ~~a~~ ~~t~~ ~~n~~ ~~p~~ ~~i~~ ~~e~~ The heat plume is not severely affected in the most severe case where the arbitrary fault is supposed to be only 4 m in the east of well (Figure 8Figure 7-b). Moving When the fault is moved on to the edge of the plume (45 m in the east: Figure 8Figure 8Figure 7-c), the heat plume appears nearly identical to that of looks almost similar to the base case. The resemblance between Similarity of Figure 8Figure 7-a and c suggests that the sealing fault's influence on the heat plume diminishes the disappearance of the sealing fault's impact on the heat plume. Surprisingly, t The heat plume is getting slightly warmer when the fault is assumed to be 48 m in west side of the well (Figure 8Figure 8Figure 7-d). Recovery curves also confirmed the slightly higher efficiency of this scenario. After injecting hot water, it flows toward the updip direction of the reservoir due to its lower density. Then, a sealing fault in the western side can prevent the flow of hot fluid from moving farther. However, over a 10-years simulation time, such localization of the reservoir can increase the performance but in a longer period, these barriers reduce the available storage space capacity of the reservoir.

Feldfunktion geändert

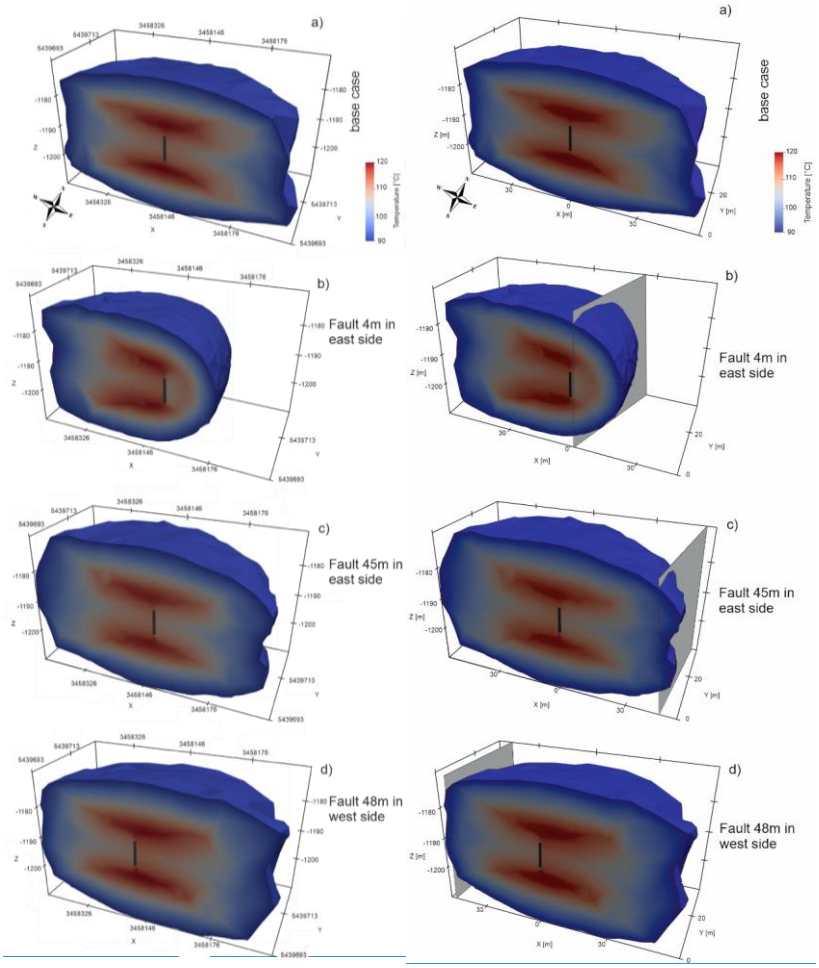

405 **Figure 87: Heat accumulation in four different scenarios of the DeepStor model at the end of the last production cycle (10 years). Planned well is shown as a solid black line. Subplots from a to d represent different scenarios including base case, arbitrary fault shown with a grey surface in 4 and 45 m in the east of the well and 48 m in the west. Temperature scale is also the same and shown only once in subplot a to avoid repetition.**

An unforeseen ~~unpredicted~~ sealing fault in the system where fluids are injected continuously may increase the pressure values dramatically. Figure 9~~Figure 8~~-a and b show a 2D section of the model and the total pressure (hydrostatic plus operation-~~caused~~ induced pressure) values across the sand reservoir after the first injection cycle. Ten injection (and production) cycles are included in the simulation and the maximum pressure increase is observed at the end of first one. The plotted trace of the pressure in Figure 9~~Figure 8~~-b is shown as a dash dotted line in the cross section of the model (~~-~~Figure 9~~Figure 8~~-a). The ~~plotted~~ pressure curves illustrate the data of four cases (to maintain figure readability~~to keep the figure readable~~) and initial condition of the trace passing through the reservoir. The pressure increase of base case at the borehole location from the initial condition to the end of first injection cycle is approximately ~~about~~ 10% (~~from~~ ~~~~11.52 MPa to 12.61 MPa). Initial condition of the model shows that pressure values ~~is~~ are distributed asymmetrically in the reservoir. ~~It~~ This distribution confirms the role of layers' inclination on pressure ~~distribution~~in the model. ~~Eastern~~ The eastern parts of the reservoir layer is dipping downward and under higher hydrostatic pressures. The pressure curve of the base case also indicates this fact by its asymmetric shape that shows a higher pressure accumulation in the eastern part of the model. This behaviour of the pressure is in contradiction to temperature that was accumulating upward. Therefore, in the majority of the faulted scenarios (14 out of 16), the arbitrary fault is located in the eastern side of the well to present the worst-case scenario that causes the highest minimum pressure. Figure 9 suggests a relation between pressure and fault distance and the pressure values decay with pressure rate. Even in worst-case scenario (fault is 4 m in the east of the well) the pressure value at the sealing fault is only 7% higher than the value in the same location of the base case. The total pressure at the fault location of worst-case (4 m) is 13.1 MPa while in base case it is 12.25 MPa. Fault surface acts as a barrier along which pressure accumulates. Figure 9-b suggests also a relation between the pressure increase and distance of the fault. ~~Note the 4 m value on the x axis of Figure 8-b to extract pressure values for the worst and base cases.~~ Figure 10~~Figure 9~~ is a contour plot of the total pressure distribution within the reservoir layer. A surface parallel to the tilted reservoir layer is chosen to ~~make~~ create this plot. The trace line shown in Figure 9~~Figure 8~~-a is extended in y direction to ~~be converted~~transform it from a line to a surface ~~and~~, making it applicable for the contour plots. In both plots, the well is located in the center with 0.0 and 0.0 coordinates. The first notable point is that pressure is accumulating alongside of the sealing fault surface. Instead of spherical pressure plumes, contour lines are proposing an elliptical high-pressure regime with major axis perpendicular to the faults surface. Despite the negligible difference in the faults' distance between Figure 10~~Figure 9~~-a and b, the pressure values are obviously higher in the case with a fault in eastern side of the well.

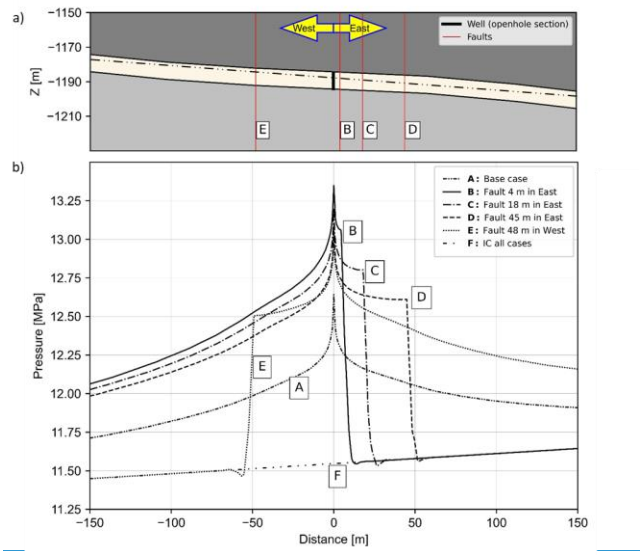
a)
West
East
Well (openhole section)
Faults
Z [m]
−1150
−1170
−1190
−1210
E
B
C
D
b)
A: Base case
B: Fault 4 m in East
C: Fault 18 m in East
D: Fault 45 m in East
E: Fault 48 m in West
F: IC all cases
Pressure [MPa]
13.25
13.00
12.75
12.50
12.25
12.00
11.75
11.50
11.25
−150
−100
−50
0
50
100
150
Distance [m]

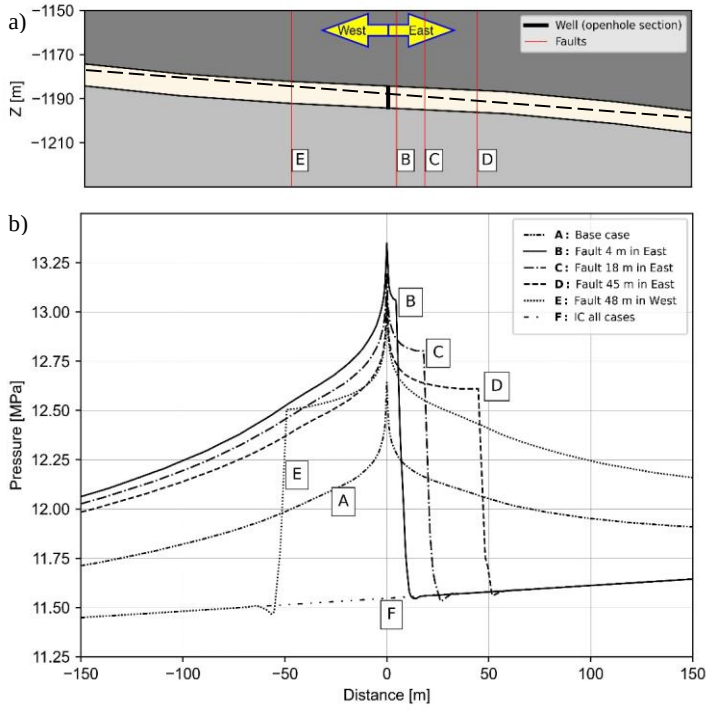

435

Figure 98: Total pressure increase of five simulated cases at the end of the first injection cycle. The cross section in subplot a indicates the position of the traces used for plotting the pressure data of five different scenarios and the initial condition (IC). Negative values for distance represent the western side of the well. To make the curves more readable, scenarios are labelled as A, B, C, D, E and the initial condition as F. ~~**This way, a visual correlation can be easily established from subplot a to b.**~~

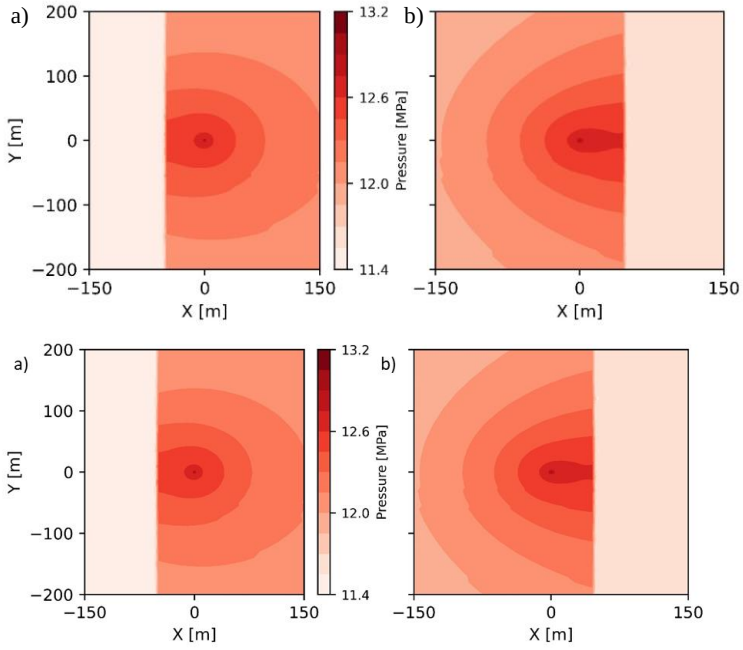

Figure 109: Total pressure changes after the first injection cycle in two scenarios. The well position is in the center of both plots (coordinates=0.0 and 0.0). Fault position is easily distinguishable by the sharp change in the pressure data: 48 m in the west of well (a) and 45 m in the east (b). Negative and positive values for x and y axis are relative to the position of the well.

The presence of the arbitrary sealing fault in DeepStor model ~~is detectable~~can be identified in the calculated pressure values from the top of the well. Figure 11~~Figure - is a plot representing~~shows the history of the total pressure values on the openhole section during first year of the HT-ATES ~~operation. A sudden change is detected in the pressure curve. The location of the fault is~~ in east (downdip of the reservoir) or west (updip) of ~~the well makes~~ the pressure response ~~makes a difference~~. Fault distance in two scenarios is the same (8 m) but in different directions from the well. Due to the downdip pressure accumulation ~~in the downdip~~, a fault with the same distance in the eastern side of the well can increase pressure more than the same one in the western side. The slight difference between solid black curve and dashed red curves is detectable in Figure 11~~Figure -~~. Additionally, ~~A~~a correlation ~~-~~between fault distance from the well and pressure increase can also be detected in this figure.

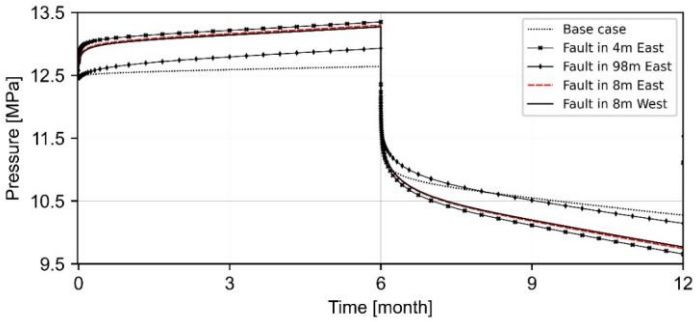

Figure 11~~10~~: Total pressure evolution in the well during the first injection and production phase. Only five cases are plotted to keep the figure readable. Higher pressure accumulation in the east of the well can be observed by the slight difference between dashed red (Fault in 8m East) and solid black (Fault in 8m West) curves.

The meshing workflow introduced here streamlines the incorporation of realistic~~facilitates including real~~ geological models and their associated uncertainties into numerical simulations. Meshing is a cumbersome step in between geological models and numerical simulators. Herein highly ~~complicated~~ complex reservoir ~~topologies~~ geometries are meshed fast and efficiently without the need for manual intervention~~any manual manipulation~~. Generation of complex surfaces, mesh refinement, embedment, and physical properties ~~attribution~~ assignment are all automated ~~for any number of cases~~. The ~~automated~~ workflow then exports ~~as much as required~~ stochastic geological meshes to cover a range of the uncertainties. This study used generic initial models and introduced arbitrary uncertainties but the developed workflow can be readily applied to real-world cases and uncertainties stemming from various data sources, such as seismic data, well logs, cores, cuttings, and others~~to them but developed workflow can be deployed for real world cases and uncertainties coming from any type of data.~~. Now, the geological models and their uncertainty can be transferred directly into reservoir simulations. This geological uncertainty later on can be applied in both the exploration and development phases. First, geologically uncertain simulations decipher the sensitivity of the results (temperature, pressure, displacement, etc.) to the perturbed parameters (~~boundaries of the~~ reservoir boundaries in ~~the~~ GGB and ~~location of the~~ sub-seismic fault location in ~~the~~ DeepStor). Second, the relation between ~~distribution of properties~~obtained results and ~~topology~~ geometry of layers can raise the importance of including real geology for the development plans. Third, in case of establishing a relation between the perturbed parameters and their outcomes, more scenarios can be generated to extend the consideration of uncertain parameters~~broaden the range of uncertainty~~. This relation can subsequently be ~~later on~~ used to update the prior knowledge based on the data collected ~~data~~ during the operation.

6.14.1 Exploration campaign design

GGB case was provided presented in this study with the purpose of detecting the possible impacts of topological geometrical uncertainty on the HT-ATES's thermal performance. While all material properties and boundary conditions in our simulations are fixed and derived from base case of a published document, the geological model, i.e., the mesh, variates. For the chosen parametrization, Results the confirmed that heat propagation plume radius even after 10 years of continuous injection and production is still about 40 m around the hot well in the thick reservoir. Introduced geometrical uncertainty to the GGB case is generic but the proposed workflow is applicable for any real case with its unique complexity/uncertainty. Upper The complex top and lower bottom surfaces of the reservoir are also hardly playing any role in the heat distribution of the thick Malm reservoir. I In contrary to this conclusion, Dashti et al. (2023) confirmed the dependence of the underground flow properties on location of the small structural elements in geological models. In the case of thin reservoirs (<20 m) also a ±10 m shift can increase/decrease the volume of the reservoir up to 50%, but thermal performance of the Malm reservoir in GGB is remained independent of such small scale thickness variations. This fact confirms the unnecessity of complex and time-consuming exploration methods for those such specific cases like GGB. Efforts for a 3D seismic campaign can intensify the exploration phase. Dedicating huge efforts to preliminary steps discourages policy makers from investing in renewable solutions like HT-ATES in settings similar to what has been assumed for GGB in this study. The GGB case clearly demonstrated that even a rough estimation of the underground surfaces is reliable enough for predicting the behaviour of the thick reservoirs at least for a 10-year snapshot. Even In some cases, existing 2D seismic slices of oilfields can bring enough accuracy for generating reliable forecasts in cases like GGB. Computationally affordable geological scenario-based analyses of geological boundariesthe reservoir can save the time dedicated to exploration.

6.24.2 Field development plan

Based on presented results for DeepStor, distribution of both the heat and pressure are tightly linked to the inclination of the thin reservoir. Therefore, incorporating realistic models into the planning process can be a critical factor in optimizing the placement of the second boreholeincluding this real model besides its uncertainty, e.g. perturbing the layer's inclination, can be a key factor in an optimum planning for the second borehole. In case of drilling the cold well with a 500 m distance from warm hot one, the negligible 5° inclination can make a 45 m difference between the depth of a horizontal and versus a tilted layer. As the next step, perturbing the depth, angle inclination and topology thickness of the layer can provide us with a range of possible depths that can be expected during the drilling of the second borehole.

Within In the URG, the majority of hydrocarbons are accumulated thanks to the existence of sealing faults. Therefore, DeepStor can also encounter these structural features. Thermohydraulic simulations revealed that only if the faults be located in thewithin distances less than the heat plume radius (45 m), can affect impact the storage successperformance. Based onConsidering the size of the heat plume, it is highly unlikely to see any effect offrom or on the Leopoldshafen or Stutensee faults on theregarding the thermal

performance of the system in a 10-year time period. The ~~T~~target sand layer is a very thin and in the case of thicker formations, ~~effect~~ impact of ~~the~~ faults can be even less important and observable.

The ~~observable~~ existing trend in Figure 11 ~~Figure 10~~ enables a primary forecast of fault distance (in case of having any) ~~merely~~ based merely on the recorded ~~pressures from the~~ borehole pressures. The pressure difference between the day five of injection and initial condition versus the distance of the fault to the well are used to formulate the forecast. It is assumed that in the day five of injection the initial reservoir condition and injection operation have reached ~~to an~~ equilibrium. This pressure value can also be ~~achieved~~ measured through ~~operating~~ a ~~separate~~ hydraulic test conducted on the well. In the base case of DeepStor, the maximum total pressure reaches from the initial 11.5 MPa to 13.3 MPa, ~~representing a 15% increase at the end of the first injection cycle~~i.e. 15% increase, at the end of injection cycle. Notably, over half of this increase (11.5 MPa to 12.5 MPa) is observed by day five of simulation. ~~Meanwhile, in the day five more than half of this increase (11.5 MPa to 12.5 MPa) is observed.~~ Figure 12 ~~Figure 11~~ shows the relation of these two variables where fault's distance from the well versus the pressure increase after five days are plotted. All the 14 black dots ~~representer~~represent the scenarios in which fault is located in the east of the well. For ~~a~~ comparison, the case with a fault in 8 m distance in west of the well is also plotted as a circle to present the pressure accumulation in the downdip. To address the ~~the~~ worst-case scenarios and be as pessimistic as possible, the forecast has been founded only on the base of the faults locating in the east side of the well. A simple exponential function with three degrees of freedom provides an acceptable level of accuracy (RMSE=0.013 MPa) for the prediction. ~~In the case of having~~With more simulations, the function can be updated to be more robust. However, we here merely try to present the possibility of formulating such simple forecast systems in a ~~complicated~~ complex reservoir. More advanced methods like machine learning can also ~~increase~~ enhance the accuracy of the prediction. Once developed, ~~Then,~~ other arbitrary distances can be fed into the predictor and the pressure value ~~in~~ on ~~the~~ day five of injection will be returned without making meshes and running the numerical simulations. ~~Meanwhile, a~~After ~~running~~ conducting the test phase in reality and measuring the ~~-~~pressure value in ~~the~~ day five of injection, the data can be inserted into the predictor to back-calculate the distance of the fault (if present~~in case of existing~~). In the case of finding discrepancies between prior assumptions about the fault's distance with output of the predictor, the geologic model can be updated. However, the ~~Validity~~ validity of this inversion scheme strongly depends on the accuracy of the chosen ~~material properties~~modelling assumptions like the material properties used (Table 1) and including only one sealing fault. Otherwise, the difference between measured and calculated pressures can originate from any other sources like petrophysical properties. Global sensitivity analyses shed light on the effect of each parameter on the response of the system. In the case of measuring material properties with error levels less than the sensitive range of the system, the proposed forecast scheme can be more reliable for predicting the underground structural model and performing independent of the parametrization.

Feldfunktion geändert

Feldfunktion geändert

Formatiert: Schriftart: 10 Pt., Nicht Fett

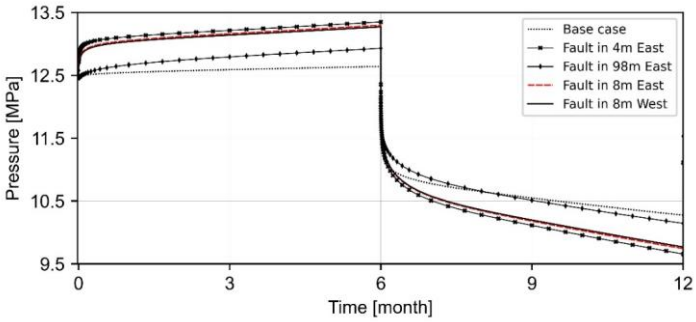

Figure 1211: Difference between borehole pressure on day five of injection and initial condition (Δ Pressure) versus the distance of the arbitrary fault to borehole. The continuous line is representing an exponential function with three degrees of freedom.

75 Conclusion

In the framework of uncertainty quantification, we have developed a tool applicable for to complex geological structures. This study demonstrates a geological scenario scenario-based analysis of HT-ATES in two showcases. A new implementation in the GMSH provided us with the possibility of creating real geological surfaces automatically to automate the generation of complicated geological surfaces rather than to overcome the manual time demanding process. The developed automated workflow in Python allows can be used to making make several meshes composed of surfaces with arbitrary shapes. The workflow also enables a fast generation of a myriad of watertightthe finite element meshes in using one single run of ablock of code in Python script. Generated meshes will link the geological uncertainty of the models to numerical simulators. We proposed used the geological uncertainty as a key input for decision-making later in different phases (exploration to development) of the HT-ATES study ranging from exploration to development.

A HT-ATES is simulated for Geneva as the second most populated city in Switzerland. In the GGB model, random geological topologies surfaces are generated to assess the sensitivity of results to the geometry of the reservoir rather than the material properties of the model with respect to the underground topology. Falling from other side of the roof in exploration plans happens when redundant levels of accuracy are demanded. GGB model clarifies this fact by showingconfirms the independence of the temperature from the geometry of the thick reservoir. The Malm layer with 100 m thickness can can possibly be detected even through 2D seismic slices and surveys. Therefore, surveys for finding the exact topology morphology of the top and bottom surfaces with higher accuracies are unnecessary for such case. This study highlights the necessity of running computationally affordable simulations prior to any exploration campaign.

The porous sand layers existing within Meletta beds beneath KIT campus are also a promising storage space. For DeepStor adding one more level of complexity (a sealing sub-seismic fault) to interpreted data expresses the performance risks such as i.e. possible significant heat losses and/or pressure increase. With the proposed material properties, the pPresented evaluation

on DeepStor proved that only in cases where a sealing fault is closer than 45 m to the well, the thermal performance of the system can be affected. The effect on the thermal recovery of the borehole is hardly observable but the overall dimension of the heat plume can change due to such faults in the vicinity (<45 m). Numerically calculated pressure values at the borehole location can decipher the faults even in 118 m distances assuming the fixed and certain petrophysical properties. ~~Relation~~ The relation between pressure changes and the location of the introduced sealing fault is used in this study to establish a case-specific ~~forecast~~ forecasting scheme for detecting possible locations of the barriers in the DeepStor model. Meanwhile, adjacency of the proposed site to oil-depleted reservoirs is a big advantage but the real experience of HT-ATES in such locations is still immature, hence first-order estimates from risk analyses need to be conducted. Further studies are required to address also the challenges associated to DeepStor including the geochemical interaction or the impact of residual hydrocarbons in the formation.

Code and data availability. GMSH can be ~~accesses~~ accessed via the published releases on the official GitLab repository at https://gitlab.onelab.info/gmsh/gmsh. Required data and developed workflows for running the model for ~~one~~ both of the showcases ~~(GGB) is~~are fully documented and available in the GitHub (https://github.com/Ali1990dashti/GeoMeshPy/tree/main/Examples/Storage_Models~~https://github.com/Ali1990dashti/GeoMeshPy/tree/main/Examples/Storag%20Model~~) and Zenodo (~~https://zenodo.org/records/10256834https://zenodo.org/record/7649506#.Y-znA3bMKUI~~) repositories of the first author.

Author contributions. AD: Conceptualization; Methodology; Simulation; Validation; Code development; Writing– original draft. JCG: Conceptualization; Geological modelling; Supervision; review & editing. CG: Code development; Writing – review & editing. FB: Geological modelling; TK: Conceptualization; Supervision; Writing – review & editing

Competing interests. The authors declare that they have no conflict of interest.

Acknowledgements. Ali Dashti is receiving the financial support from The German Academic Exchange Service (Deutscher Akademischer Austauschdienst: DAAD) to do his PhD in Germany as the Research Grants-Doctoral programmes in Germany 2019/20. This organization is appreciated for giving the opportunity to researchers. The study is also part of the Helmholtz portfolio project Geoenergy. The support from the program “Renewable Energies”, under the topic “Geothermal Energy Systems”, is gratefully acknowledged. The authors are grateful to Prof. Guillaume Caumon and Prof. Florian Wellmann for their insightful reviews and comments that significantly improved the quality of this manuscript. Authors appreciate the support of Prof. Eva Schill (eva.schill@kit.edu) for the data availability and geological model of the DeepStor. Dr. Denise Degen (denise.degen@cgre.rwth-aachen.de) is appreciated due to her support and constructive comments. Fruitful comments of Kai R. Stricker (kai.stricker@kit.edu) regarding the numerical modelling section are wholeheartedly acknowledged.

86 References

Agemar, T., Schellschmidt, R., and Schulz, R.: Subsurface temperature distribution in Germany, Geothermics, 44, 65–77, https://doi.org/10.1016/j.geothermics.2012.07.002, 2012.

Baillieux, P., Schill, E., Edel, J.-B., and Mauri, G.: Localization of temperature anomalies in the Upper Rhine Graben: insights from geophysics and neotectonic activity, International Geology Review, 55, 1744–1762, https://doi.org/10.1080/00206814.2013.794914, 2013.

Birdsell, D. T. and Saar, M. O.: Modeling Ground Surface Deformation at the Swiss HEATSTORE Underground Thermal Energy Storage Sites, 22046, 2020.

Bloemendal, M., Olsthoorn, T., and Boons, F.: How to achieve optimal and sustainable use of the subsurface for Aquifer Thermal Energy Storage, Energy Policy, 66, 104–114, https://doi.org/10.1016/j.enpol.2013.11.034, 2014.

Böcker, J., Littke, R., and Forster, A.: An overview on source rocks and the petroleum system of the central Upper Rhine Graben, Int J Earth Sci (Geol Rundsch), 106, 707–742, https://doi.org/10.1007/s00531-016-1330-3, 2017.

Böhm, H. and Lindorfer, J.: Techno-economic assessment of seasonal heat storage in district heating with thermochemical materials, Energy, 179, 1246–1264, https://doi.org/10.1016/J.ENERGY.2019.04.177, 2019.

Bond, C. E.: Uncertainty in structural interpretation: Lessons to be learnt, Journal of Structural Geology, 74, 185–200, https://doi.org/10.1016/j.jsg.2015.03.003, 2015.

Caers, J.: Modeling Uncertainty in the Earth Sciences, John Wiley & Sons, Ltd, Chichester, UK, 2011.

Chelle-Michou, C., Do Couto, D., Moscariello, A., Renard, P., and Rusillon, E.: Geothermal state of the deep Western Alpine Molasse Basin, France-Switzerland, Geothermics, 67, 48–65, https://doi.org/10.1016/j.geothermics.2017.01.004, 2017.

Chevalier, G., Diamond, L. W., and Leu, W.: Potential for deep geological sequestration of CO2 in Switzerland: a first appraisal, Swiss J Geosci, 103, 427–455, https://doi.org/10.1007/s00015-010-0030-4, 2010.

Collignon, M., Klemetsdal, Ø. S., Møyner, O., Alcanié, M., Rinaldi, A. P., Nilsen, H., and Lupi, M.: Evaluating thermal losses and storage capacity in high-temperature aquifer thermal energy storage (HT-ATES) systems with well operating limits: insights from a study-case in the Greater Geneva Basin, Switzerland, Geothermics, 85, 101773, https://doi.org/10.1016/j.geothermics.2019.101773, 2020.

Damsleth, E., Sangolt, V., and Aamodt, G.: Sub-seismic Faults Can Seriously Affect Fluid Flow in the Njord Field off Western Norway - A Stochastic Fault Modeling Case Study, in: All Days, New Orleans, Louisiana, 9/27/1998 - 9/30/1998, 1998.

Dashti, A., Gholami Korzani, M., Geuzaine, C., Egert, R., and Kohl, T.: Impact of structural uncertainty on tracer test design in faulted geothermal reservoirs, Geothermics, 107, 102607, https://doi.org/10.1016/j.geothermics.2022.102607, 2023.

Dèzes, P., Schmid, S. M., and Ziegler, P. A.: Evolution of the European Cenozoic Rift System: interaction of the Alpine and Pyrenean orogens with their foreland lithosphere, Tectonophysics, 389, 1–33, https://doi.org/10.1016/j.tecto.2004.06.011, 2004.

Dinkelman, D. and van Bergen, F. (Eds.): Evaluation of the country-wide potential for High-Temperature Aquifer Thermal Energy Storage (HT-ATES) in the Netherlands, 2022.

Faleide, T. S., Braathen, A., Lecomte, I., Mulrooney, M. J., Midtkandal, I., Bugge, A. J., and Planke, S.: Impacts of seismic resolution on fault interpretation: Insights from seismic modelling, Tectonophysics, 816, 229008, https://doi.org/10.1016/j.tecto.2021.229008, 2021.

Feng, R., Grana, D., and Balling, N.: Uncertainty quantification in fault detection using convolutional neural networks, GEOPHYSICS, 86, M41-M48, https://doi.org/10.1190/geo2020-0424.1, 2021.

Fleuchaus, P., Schüppler, S., Bloemendal, M., Guglielmetti, L., Opel, O., and Blum, P.: Risk analysis of High-Temperature Aquifer Thermal Energy Storage (HT-ATES), Renewable and Sustainable Energy Reviews, 133, 110153, https://doi.org/10.1016/j.rser.2020.110153, 2020a.

Fleuchaus, P., Schüppler, S., Godschalk, B., Bakema, G., and Blum, P.: Performance analysis of Aquifer Thermal Energy Storage (ATES), Renewable Energy, 146, 1536–1548, https://doi.org/10.1016/j.renene.2019.07.030, 2020b.

Fleuchaus, P., Godschalk, B., Stober, I., and Blum, P.: Worldwide application of aquifer thermal energy storage – A review, Renewable and Sustainable Energy Reviews, 94, 861–876, https://doi.org/10.1016/j.rser.2018.06.057, 2018.

Gao, L., Zhao, J., An, Q., Liu, X., and Du, Y.: Thermal performance of medium-to-high-temperature aquifer thermal energy storage systems, Applied Thermal Engineering, 146, 898–909, https://doi.org/10.1016/j.applthermaleng.2018.09.104, 2019.

Gaston, D., Newman, C., Hansen, G., and Lebrun-Grandié, D.: MOOSE: A parallel computational framework for coupled systems of nonlinear equations, Nuclear Engineering and Design, 239, 1768–1778, https://doi.org/10.1016/j.nucengdes.2009.05.021, 2009.

Geuzaine, C. and Remacle, J.-F.: Gmsh: A 3-D finite element mesh generator with built-in pre- and post-processing facilities, Int. J. Numer. Meth. Engng., 79, 1309–1331, https://doi.org/10.1002/nme.2579, 2009.

Gholami Korzani, M., Held, S., and Kohl, T.: Numerical based filtering concept for feasibility evaluation and reservoir performance enhancement of hydrothermal doublet systems, Journal of Petroleum Science and Engineering, 190, 106803, https://doi.org/10.1016/j.petrol.2019.106803, 2020.

Glubokovskikh, S., Saygin, E., Shapiro, S., Gurevich, B., Isaenkov, R., Lumley, D., Nakata, R., Drew, J., and Pevzner, R.: A Small CO 2 Leakage May Induce Seismicity on a Sub-Seismic Fault in a Good-Porosity Clastic Saline Aquifer, Geophys. Res. Lett., 49, https://doi.org/10.1029/2022GL098062, 2022.

Gong, L., Liu, B., Fu, X., Jabbari, H., Gao, S., Yue, W., Yuan, H., Fu, R., and Wang, Z.: Quantitative prediction of sub-seismic faults and their impact on waterflood performance: Bozhong 34 oilfield case study, Journal of Petroleum Science and Engineering, 172, 60–69, https://doi.org/10.1016/j.petrol.2018.09.049, 2019.

Green, S., McLennan, J., Panja, P., Kitz, K., Allis, R., and Moore, J.: Geothermal battery energy storage, Renewable Energy, 164, 777–790, https://doi.org/10.1016/j.renene.2020.09.083, 2021.

Grimmer, J. C., Ritter, J. R. R., Eisbacher, G. H., and Fielitz, W.: The Late Variscan control on the location and asymmetry of the Upper Rhine Graben, Int J Earth Sci (Geol Rundsch), 106, 827–853, https://doi.org/10.1007/s00531-016-1336-x, 2017.

Guglielmetti, L., Heidinger, M., Eichinger, F., and Moscariello, A.: Hydrochemical Characterization of Groundwaters' Fluid Flow through the Upper Mesozoic Carbonate Geothermal Reservoirs in the Geneva Basin: An Evolution more than 15,000 Years Long, Energies, 15, 3497, https://doi.org/10.3390/en15103497, 2022.

Harris, R., Bracken, K., Miller, B., Angelovich, S., and O'Toole, T.: Subseismic Fault Identification Using the Fault Likelihood Attribute: Application to Geosteering in the DJ Basin, in: Proceedings of the 7th Unconventional Resources Technology Conference, Denver, Colorado, USA, 7/22/2019 - 7/24/2019, 2019.

Kuhlemann, J. and Kempf, O.: Post-Eocene evolution of the North Alpine Foreland Basin and its response to Alpine tectonics, Sedimentary Geology, 152, 45–78, https://doi.org/10.1016/S0037-0738(01)00285-8, 2002.

Li, Z., Dong, M., Li, S., and Huang, S.: CO2 sequestration in depleted oil and gas reservoirs—caprock characterization and storage capacity, Energy Conversion and Management, 47, 1372–1382, https://doi.org/10.1016/j.enconman.2005.08.023, 2006.

Lindsay, A. D., Gaston, D. R., Permann, C. J., Miller, J. M., Andrš, D., Slaughter, A. E., Kong, F., Hansel, J., Carlsen, R. W., Icenhour, C., Harbour, L., Giudicelli, G. L., Stogner, R. H., German, P., Badger, J., Biswas, S., Chapuis, L., Green, C., Hales, J., Hu, T., Jiang, W., Jung, Y. S., Matthews, C., Miao, Y., Novak, A., Peterson, J. W., Prince, Z. M., Rovinelli, A., Schunert, S., Schwen, D., Spencer, B. W., Veeraraghavan, S., Recuero, A., Yushu, D., Wang, Y., Wilkins, A., and Wong, C.: 2.0 - MOOSE: Enabling massively parallel multiphysics simulation, SoftwareX, 20, 101202, https://doi.org/10.1016/j.softx.2022.101202, 2022.

Mahon, H., O'Connor, D., Friedrich, D., and Hughes, B.: A review of thermal energy storage technologies for seasonal loops, Energy, 239, 122207, https://doi.org/10.1016/j.energy.2021.122207, 2022.

Mindel, J. and Driesner, T.: HEATSTORE: Preliminary Design of a High Temperature Aquifer Thermal Energy Storage (HT-ATES) System in Geneva Based on TH Simulations, 2020.

Muhammed, N. S., Haq, M. B., Al Shehri, D. A., Al-Ahmed, A., Rahman, M. M., Zaman, E., and Iglauer, S.: Hydrogen storage in depleted gas reservoirs: A comprehensive review, Fuel, 337, 127032, https://doi.org/10.1016/j.fuel.2022.127032, 2023.

Open CASCADE Technology, https://www.opencascade.com.

Pasquinelli, L., Felder, M., Gulbrandsen, M. L., Hansen, T. M., Jeon, J.-S., Molenaar, N., Mosegaard, K., and Fabricius, I. L.: The feasibility of high-temperature aquifer thermal energy storage in Denmark: the Gassum Formation in the Stenlille structure, bgsd, 68, 133–154, https://doi.org/10.37570/bgsd-2020-68-06, 2020.

Pribnow, D. and Schellschmidt, R.: Thermal tracking of upper crustal fluid flow in the Rhine graben, Geophys. Res. Lett., 27, 1957–1960, https://doi.org/10.1029/2000GL008494, 2000.

Reinhold, C., Schwarz, M., and Perner, M.: The Northern Upper Rhine Graben re-dawn of a mature petroleum province?, https://doi.org/10.5169/seals-658196, 2016.

Réveillère, A., Hamm, V., Lesueur, H., Cordier, E., and Goblet, P.: Geothermal contribution to the energy mix of a heating network when using Aquifer Thermal Energy Storage: Modeling and application to the Paris basin, Geothermics, 47, 69–79, https://doi.org/10.1016/j.geothermics.2013.02.005, 2013.

Rotevatn, A. and Fossen, H.: Simulating the effect of subseismic fault tails and process zones in a siliciclastic reservoir analogue: Implications for aquifer support and trap definition, Marine and Petroleum Geology, 28, 1648–1662, https://doi.org/10.1016/j.marpetgeo.2011.07.005, 2011.

Rybach, L.: Geothermal potential of the Swiss Molasse basin, 1992.

Schmidt, T., Pauschinger, T., Sørensen, P. A., Snijders, A., Djebbar, R., Boulter, R., and Thornton, J.: Design Aspects for Large-scale Pit and Aquifer Thermal Energy Storage for District Heating and Cooling, Energy Procedia, 149, 585–594, https://doi.org/10.1016/j.egypro.2018.08.223, 2018.

Schumacher, M. E.: Upper Rhine Graben: Role of preexisting structures during rift evolution, Tectonics, 21, 6-1-6-17, https://doi.org/10.1029/2001TC900022, 2002.

Stricker, K., Grimmer, J. C., Egert, R., Bremer, J., Korzani, M. G., Schill, E., and Kohl, T.: The Potential of Depleted Oil Reservoirs for High-Temperature Storage Systems, Energies, 13, 6510, https://doi.org/10.3390/en13246510, 2020.

Thore, P., Shtuka, A., Lecour, M., Ait-Ettajer, T., and Cognot, R.: Structural uncertainties: Determination, management, and applications, GEOPHYSICS, 67, 840–852, https://doi.org/10.1190/1.1484528, 2002.

Wang, Q., Shi, W., Zhan, H., and Xiao, X.: New model of Single-Well Push-Pull thermal test in a Fracture-Matrix system, Journal of Hydrology, 585, 124807, https://doi.org/10.1016/j.jhydrol.2020.124807, 2020.

Wellmann, F. and Caumon, G.: 3-D Structural geological models: Concepts, methods, and uncertainties, Elsevier, 1–121, https://doi.org/10.1016/bs.agph.2018.09.001, 2018.

Wellmann, J. F. and Regenauer-Lieb, K.: Uncertainties have a meaning: Information entropy as a quality measure for 3-D geological models, Tectonophysics, 526-529, 207–216, https://doi.org/10.1016/j.tecto.2011.05.001, 2012.

Wellmann, J. F., Horowitz, F. G., Schill, E., and Regenauer-Lieb, K.: Towards incorporating uncertainty of structural data in 3D geological inversion, Tectonophysics, 490, 141–151, https://doi.org/10.1016/j.tecto.2010.04.022, 2010.

Wesselink, M., Liu, W., Koornneef, J., and van den Broek, M.: Conceptual market potential framework of high temperature aquifer thermal energy storage - A case study in the Netherlands, Energy, 147, 477–489, https://doi.org/10.1016/j.energy.2018.01.072, 2018.

Wirth, E.: Die Erdöllagerstätten Badens, Abh. Geol. Landesamt Baden-Württemberg: Freiburg, Germany, 4, 63–80, 1962.